ACCSCIENCE PUBLISHING

Engineering Science in Additive Manufacturing

ORIGINAL RESEARCH ARTICLE

Mechanical properties and energy absorption capability improvement of Ti-6Al-4V porous materials through porous structure design optimization

Yu-Yao Chan, Yi Chao, and Che-Nan Kuo*

Department of Materials and Optoelectronic Science, National Sun Yat-sen University, Kaohsiung, Taiwan, Republic of China

Abstract

The structural materials, which exhibit high toughness and high strain energy absorption, can be used in impact-resistant applications such as bulletproof vests, automobiles, and aerospace. Numerous studies indicate that functional gradient materials, which contain non-uniform density, exhibit excellent performance in energy absorption. During the compression test, the struts of the gradient porosity materials collapsed layer by layer, and this phenomenon optimizes the energy absorption capability of the materials. Furthermore, the collapse region or direction can be predicted and controlled by the design of the gradient porosity materials. In addition to the above concepts, this research also improves its energy absorption capacity through the following two strategies: (1) Chamfering the node of the porous structure to avoid the stress concentration, and (2) optimizing the angle between the struts of the porous material to enhance the ductility of the material. To fabricate the complicated gradient porosity structure, the structural materials were printed using the selective laser melting process with Ti-6Al-4V ELI alloys. Through the experiments conducted in this study, the structural strength was enhanced by up to 28% through structure design, and the energy absorption was improved by 19% compared to the gyroid structure, which has been reported to exhibit good energy absorption capabilities.

Keywords: Energy absorption; Ti-6Al-4V; Chamfering design; Selective laser melting; Lattice structure design

***Corresponding author:**
Che-Nan Kuo
(cnkuo@mail.nsysu.edu.tw)

Citation: Chan Y, Chao Y, Kuo C. Mechanical properties and energy absorption capability improvement of Ti-6Al-4V porous materials through porous structure design optimization. *Eng Sci Add Manuf*. 2025;1(2):025170009. doi: 10.36922/ESAM025170009

Received: April 21, 2025

Revised: May 8, 2025

Accepted: May 20, 2025

Published online: June 17, 2025

1. Introduction

Ti-6Al-4V is a high-strength, low-density α+β phase titanium alloy exhibiting superior strength, corrosion resistance, and excellent biocompatibility.[1,2] Compared to other common metallic alloys (Table 1), Ti-6Al-4V results in higher specific strength,[3,4] widely utilized as a lightweight alloy. In addition to reducing weight by altering material properties, lightweight can also be achieved through structural design. Porous structures are commonly used in lightweight structural designs; it can not only maintain the strength of materials but also save materials, energy consumption, and manufacturing time effectively.[5-7] Besides, porous structures with high specific strength,

Table 1. Mechanical properties comparison of common metallic alloys

Material	Density (g/cm^3)	Compressive strength (MPa)	Specific strength (MPa·cm^3/g)	Strain (%)	Hardness (MPa)	Young's modulus (GPa)
Steel 4340	7.85	470	59.9	22	228	205
Ti6Al4V	4.43	1080	243.8	18	349	113
AlSc	2.67	474	107.5	20	115	72
CuNi	8.90	550	61.8	23	160	162

excellent energy absorption ability, and outstanding vibration-damping characteristics have demonstrated significant application in modern engineering, such as the automobile, aerospace, and defense industries.[8] For example, in the automobile industry, porous structures are utilized in the manufacture of crash energy absorption components, enhancing passenger safety and comfort;[9,10] in the aerospace sector, porous structures are applied in aircraft structural components to reduce weight and improve fuel efficiency;[11,12] in defense applications, porous structures are commonly used in energy-absorbing armor and lightweight vehicle shells, increasing their ability to absorb impact energy.[13] With design flexibility and multifunctionality, porous structures have become indispensable elements in materials engineering and structural design, continually driving the development of high-performance materials.

Porous structures can be classified into three categories: Foam (open-cell and closed-cell), honeycomb, and lattice structures. Lattice structures are composed of an array of spatial units, with each unit's shape and size being either uniform or non-uniform. Compared to foam and honeycomb structures, lattice structures exhibit better mechanical performance and have the potential to enhance compressive strength.[14-16]

Conventional manufacturing methods, such as metallic foam production, have been widely used to fabricate porous metal structures. However, these methods typically result in random, non-uniform pore architectures, making it difficult to precisely control key parameters such as strut orientation, porosity distribution, and overall geometry. Furthermore, substantial material consumption through processes such as forging, casting, and rolling are limited in producing complex shapes and are associated with high production costs and lengthy process times. To address this situation, additive manufacturing can be utilized. Additive manufacturing, also known as 3D printing, allows for the rapid production of complex geometric shapes by printing the product layer by layer.[17,18] The product's shape is based on computer-aided design (CAD) models generated by computer software. Powder bed fusion is one of the additive manufacturing technologies commonly used for metal components and can be categorized into electron beam melting (EBM) and selective laser melting (SLM). EBM employs an electron beam as the heat source, whereas SLM utilizes a laser. In this process, the metal powder on the molten powder bed is scanned according to the modeling, and the metal parts are formed by superposition layer by layer.[18] SLM features finer powder particles and a smaller melt pool, enabling the fabrication of parts with high geometric complexity and fine structural features. Moreover, the melt pool exhibits a higher cooling rate and promotes samples with higher mechanical strength.[19-21] The quality of additive manufacturing samples and the microstructure of materials will be affected by various processing parameters, such as scanning speed, laser power, hatch distances, and layer thickness.

As materials for energy absorption structures, they need to exhibit characteristics such as high strength and high ductility.[22] The mechanical properties and energy absorption effectiveness of materials can be calculated by compression testing and energy absorption formulas (specific energy absorption [SEA]). Material toughness is defined as the energy absorbed per unit volume before fracture. Toughness is related to the area under the stress–strain curve, with a larger area indicating better toughness, meaning the material must be both strong and ductile.[23] Compression testing provides the strength and strain of the material, and further calculation using Equation I determines how much energy the material can absorb before fracture.

$$\text{Specific energy absorption } (\text{J/g}) = \frac{\int_0^{\epsilon d} \sigma \, d\epsilon}{\rho} \quad \text{(I)}$$

where ρ represents the material density; σ represents the stress experienced by the material at strain ϵ; and ϵ_d represents the densification strain of the material. The unit of SEA is Joule/gram (J/g). From Equation I, it can be deduced that if the density of the material is smaller, under the same strength and ductility, the energy absorption capacity per unit weight will be higher. In other words, materials with high specific strength alloys and low-density porous structures will contribute to enhancing the capability of energy absorption during deformation.

On the other hand, data obtained from compression experiments on gradient materials show that due to the

layered pore distribution in gradient materials, the material collapses layer by layer during the collapse process instead of immediately fracturing along the direction of maximum shear force at approximately 45° from top to bottom. In addition, during the collapse process, densification stacking occurs, resulting in a higher area under the stress–strain curve for gradient materials compared to uniform density; this characteristic provides better energy absorption for gradient materials.[23-25]

In additive manufacturing, products made by SLM typically exhibit a very rough surface, often with many incompletely melted powders adhering to the surface. From a microscopic perspective, when subjected to an external force, stress concentrates at the tip of cracks. Cracks with smaller curvature radius and deeper notches experience a rapid increase in strength, causing them to withstand greater strength than other locations. Consequently, they are more likely to exceed the yield strength and plastic deformation that happened earlier. This phenomenon initiates the propagation of cracks from pre-existing flaws, resulting in material fracture, accompanied by a decrease in both strength and ductility.[26] Stress concentration can be expressed as follows (Equation II):

$$\sigma_{max} = \sigma \times (1 + 2\sqrt{\frac{d}{\rho}}) \quad \text{(II)}$$

where σ_{max} is the stress at the notch, σ is the applied stress, ρ is the curvature radius of the notch, and d is the distance from the notch tip to the surface.

Another study adopts the lattice structures with smooth surfaces based on the mathematical approach of triply periodic minimal surface (TPMS). TPMS is a class of minimal surfaces that exhibit periodicity in three-dimensional space and possess zero mean curvature at every point on the surface. Common types of TPMS structures include the gyroid, diamond, and Schwarz-Primitive surfaces, which can be mathematically defined through equations or parametric modeling.[27] With the advancement of additive manufacturing technologies, the complex geometries of TPMS structures can now be fabricated using 3D printing. TPMS structures demonstrate excellent mechanical properties and fluid permeability.[28,29] Optimizing the nodes of the struts causes changes in strength distribution, which significantly impacts the deformation behavior of the structure. This optimization can result in the structure standing more strength distribution, thereby increasing its strength.[30] The volume fraction is a crucial parameter controlling the mechanical properties of porous materials, and it can be determined by the strut diameter, optimized radius, and lattice size. When the unit size is set as a constant, increasing the strut diameter can rapidly increase the volume fraction, and the porosity of the structure will decrease to achieve the desired mechanical properties. The influence of the optimized radius on the volume fraction is presented in the stiffness and strength of the material structure, both of which are significantly enhanced.[26]

When a material is subjected to perpendicular strength, it may undergo deformation, which can be classified into two types: "bending" and "buckling." Bending occurs due to the strain behavior induced in the material by strength applied perpendicular to its principal axis, whereas buckling refers to a sudden change in the shape of the material when axial strength reaches a critical level.[31-33] This study focuses on the relationship between material strength and Young's modulus by exploring the effects of buckling and bending deformations of struts. Zhao *et al.*[34] conducted with Cubic, G7, and Rhombic dodecahedron. The results indicate that the Cubic structure mostly fractures due to compressive strength, mainly compressed by perpendicular buckling struts. On the other hand, for the G7 and Rhombic dodecahedron structures, strength is mainly compressed by bending struts under tension and compression. Through the design of strut shapes, increasing the number of buckling struts can increase the ultimate fatigue strength of the material. Conversely, an increase in bending struts prompts the material to develop fatigue cracks. The growth of fatigue cracks within the struts significantly affects the material, accelerating its fracture.

The gyroid structure is based on a TPMS. Due to its smooth surface, the gyroid structure exhibits high ductility and has been the subject of numerous studies indicating its high energy absorption capabilities.[35,36] According to the above conception, the structure with rounded corners can reduce the stress concentration at the node, and the vertical strut, which is parallel to the compression direction, can be separated by bending and buckling vector, enhancing the buckling vector could enhance the strength and ductility of the structure. Both of them can enhance the capability of energy absorption. However, the gyroid structure is already smooth enough and without any vertical struts, which means that it is difficult to improve the performance of the gyroid structure through the design optimization described above.[37] Hence, in this study, we would like to explore the performance improvement capability of tetrahedron structure[38] and compare it with the control group of gyroid structures, whose mechanical properties are reportedly better than that of tetrahedron structure. Moreover, only the relationship between structures with rounded corners and varying structural angles was explored in previous studies. Thus, this study only revealed the different angles between the struts, and research on the

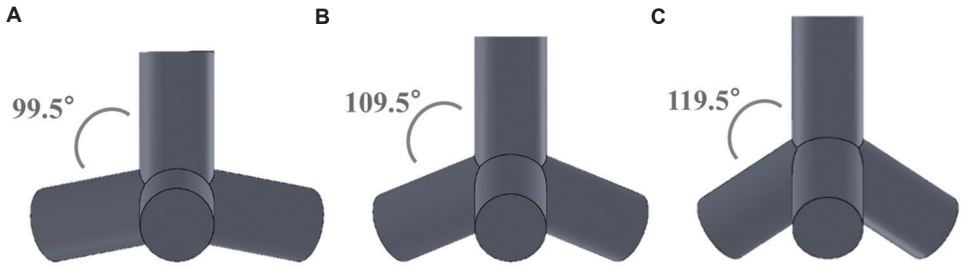

Figure 1. The CAD model of porous materials with different angles between the struts was designed by SolidWorks. The tetrahedral unit cell of different angles between the struts (A) 99.5°, (B) 109.5°, and (C) 119.5°.
Abbreviation: CAD: Computer-aided design.

rounded corner will be conducted in future studies. The current study also attempted to discuss the compression behavior and mechanical properties with different angles between the struts. The effects of rounded corners and varying strut angles in structures fabricated by SLM warrant further investigation. This study introduced and optimized the tetrahedral structure through three key strategies, including: (1) Optimization of the angles between the struts of the porous materials, (2) node chamfering of the porous materials, and (3) introduction of porosity gradient into the porous materials. During the mechanical test, the compression direction was fixed through the z-axis by the specimen. Then, how the angle between the struts and structure with rounded corners affects the capability of energy absorption was discussed. Meanwhile, the characteristics and mechanical properties of the gradient porosity materials with these two variables (rounded corners and different angles between the struts) are cautiously investigated and discussed.

2. Materials and methods

The experiment was conducted with Ti-6Al-4V powder manufactured by a domestic metal powder manufacturer (Chung Yo Materials, Taiwan), using the vacuum induction gas atomization (VIGA) method. The powder size distribution was D10 of 27 m, D50 of 38 m, and D50 of 49 m.

In this study, specimens were designed by SolidWorks with different angles of the unit cell, and the porosity of the material was varied by changing the diameters of the struts. For the tetrahedral structure in the diamond lattice, we constructed the CAD model along the z-axis, aligning the vertical struts parallel to the compressive loading direction. Then, the structure angle between the struts from its standard 109.5° was adjusted through increasing/decreasing by 10°. This modification allows us to discuss the different mechanical behavior under different angles between the struts. Initially, SolidWorks was used to draw tetrahedral unit cells with angles of 99.5°, 109.5°, and

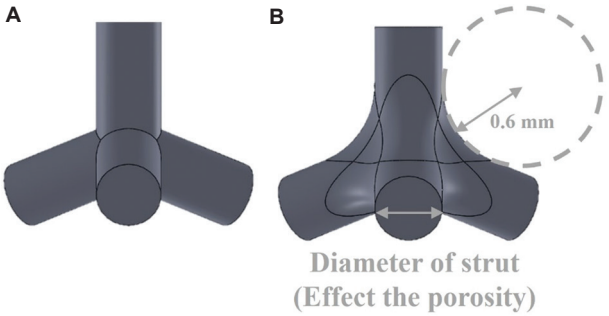

Figure 2. Demonstration of tetrahedral CAD unit cell (A) without and (B) with rounded corners
Abbreviation: CAD: Computer-aided design.

119.5° (Figure 1) and the unit cell with rounded corners or not (Figure 2). Then, the gradient structure was designed by Magics software; after designing the CAD model, the unit cells were imported into Magics and filled to create a cylinder with a diameter of 18 mm and a height of 36 mm. To prevent damage from the compression platen during compression, 1 mm thick disks were designed at the top and bottom to protect the specimens. Then, it was sliced layer by layer and exported as files that can be read by 3D printing machines.

When designing the gradient material, adjusting the thickness of the struts of each unit cell allows for adjustment of its volume fraction. Through the calculation of porosity, different gradient structures with varying porosities can be designed. In this study, specimens were divided into five gradients: 55%, 60%, 65%, 70%, and 75%. To maintain a width-to-height ratio of 1:2 and an average porosity of 65% for the middle layer and to be compared with the original single porosity of 65%, each porosity was designed to have a height ratio of 1:1:1.5:1:1 (Figure 3). Each specimen was printed in five copies to ensure the accuracy and reproducibility of the experimental data (Figure 4).

In this study, the naming of the specimens accords with the following rules. "O" signifies original design, indicating structures without rounded corners. "R" stands for

rounded, representing structures with rounded corners. The numerical values, such as 99.5/109.5/119.5 denote different structural angles. In addition, "65" indicates uniform porosity at 65%, and "G" is used for gradient porosity, 55% – 60% – 65% – 70% – 75%.

The specimens used in this experiment were all printed using the SolidMEN AM300 printer from the Industrial Technology Research Institute. To minimize powder waste and save time, a resource-based view restriction module was added to the machine, limiting the size of the build platform to 120 mm × 120 mm. This equipment utilizes SLM technology, and the scanning parameters are set according to Table 2. The chamfer was filled with argon gas

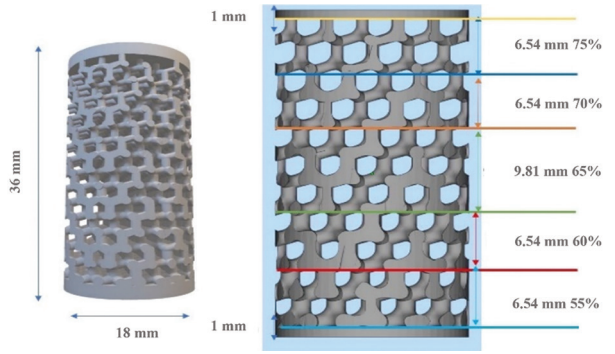

Figure 3. CAD model of cylinder specimen R_109.5_G (55% – 60% – 65% – 70% – 75%). Each porosity was designed in a height ratio of 1:1:1.5:1:1 to maintain an average porosity of 65%.
Abbreviation: CAD: Computed-aided design.

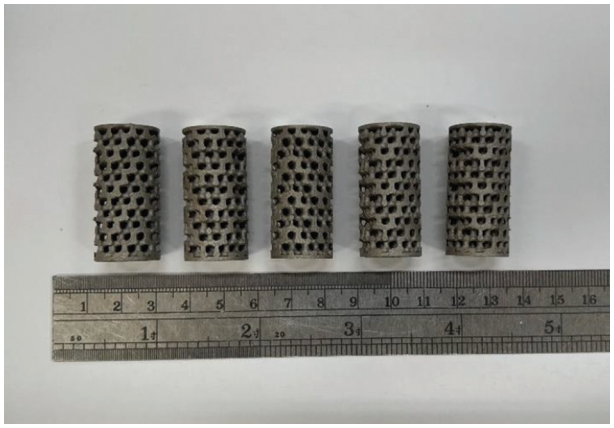

Figure 4. Five specimens in each group of samples. To ensure the accuracy and reproducibility of the test, the sample was printed by selective laser melting, with only the top and bottom surfaces subject to grinding. The image shows the representative sample O_109.5_65.

Table 2. Selective laser melting printing parameters of this study

Laser power	Scan speed	Layer thickness	Hatch distance
100 W	1087.5 mm/s	0.03 mm	0.081 mm

to provide environmental protection, preventing reactions between the samples and oxygen during fabrication.

To ensure that the porosity of the printed sample is the same as the designed CAD model, the density and the weight of the printed sample need to be calculated. Using Equation III, the porosity can be calculated:

$$\rho = (1 - \frac{V}{V_0}) \times 100\% \quad \text{(III)}$$

where ρ is the material porosity, V is the material real volume, and V_0 is the volume of a cylinder. The primary objective of compression testing is to determine the material's behavior and mechanical properties under compression by measuring fundamental variables such as strength and deformation. The compression test would be conducted with an Instron 5582 Universal testing machine (Instron, United States) at an initial strain rate of 1×10^{-4} (s^{-1}). To ensure the strain accurately from the specimen, a linear variable differential transformer was externally attached at room temperature. During compression testing, the test specimen was placed between two platens, and compression was applied using a crosshead to control displacement. Typically, the specimen would be shortening along the compression force direction while expanding outward in the perpendicular direction. Stress–strain curves were plotted using Origin software to analyze Young's modulus, yield strength, compression strength, and SEA, facilitating an assessment of the material's energy absorption capability.

To observe whether the printed specimens match the designed strut angles and to calculate the radius of curvature of the rounded corner specimens, the specimens were cut into longitudinal sections using a grinding machine operating at 2500 rpm with a feed rate of 2.5 mm/min. For further validation, image analysis software such as ImageJ was utilized to calculate the radius of curvature of the notches based on images captured using both optical and electron microscopes. Each experimental sample was sectioned, and 3 – 5 images were captured using optical microscopy for analysis with ImageJ. The optical microscope used in the experiment was Leica DM750 (Leica Microsystems, Germany), whereas the electron microscope was a tabletop model Phenom Pro XG6 (Thermo Fisher Scientific, United States).

3. Results and discussion

3.1. Measurement of specimen and microstructure analysis

After designing the specimens, the weight of the printed specimens can be measured, and the thickness of the small

Table 3. Design porosity and measurement porosity of the specimen in this study

Specimen	Design porosity (%)	Measurement porosity (%)	Deviation (%)
O_99.5_65	65.00	66.28±0.18	1.96
O_109.5_65	65.00	65.62±0.09	0.95
O_119.5_65	65.00	65.63±0.23	0.97
R_99.5_65	65.00	66.19±0.05	1.02
R_109.5_65	65.00	65.05±0.27	0.08
R_119.5_65	65.00	65.46±0.16	0.71

Note: All the porosity data were measured and calculated using Equation III.

discs can be measured by caliper. Then, the weights of the upper and lower small discs were subtracted, and the density was calculated to determine the actual porosity of the specimens. A comparison between the experimental porosity and the computer-designed porosity is shown in Table 3. According to Table 3, it can be observed that the experimental porosity is within 2% of the design porosity, indicating a close match.

Image analysis software such as ImageJ was used to observe whether the angle of the printed structure is consistent with the design. The demonstration of the measurement method is shown in Figure 5. Under the optical microscope, a large amount of unmelted powder adhered to the structure can be observed, causing roughness on the surface of the struts.

3.2. Impact of chamfer design on mechanical properties

According to the experimental results in Table 4 and Figure 6, it can be observed that structures with rounded corners have higher yield strength and compressive strength compared to structures without rounded corners.[39] Specifically, the yield strength was increased by approximately 8% and the compressive strength by about 6%. However, the improvement was only marginal compared to the effect of manipulating the angle between the struts, indicating that the influence of node with chamfer or not on mechanical properties was less significant.

Analyzing the specimens under a microscope and using ImageJ, we can measure the depth (d) and curvature radius (ρ) of the strut notches. By applying the stress concentration formula, we can calculate the maximum strength of the notch. The depth and curvature radius of the notch with and without rounded corners are depicted in Figure 7.

The results based on Equation II are summarized in Table 5. For structures without rounded corners, the strength stand by the notch (σ_{max}) under a force of F was significantly higher compared to structures with rounded

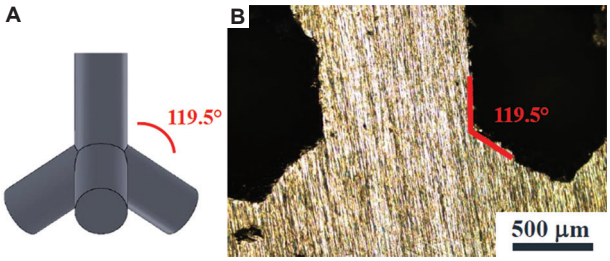

Figure 5. Demonstration of the angle between the struts in (A) CAD model and (B) analysis by ImageJ
Abbreviation: CAD: Computer-aided design.

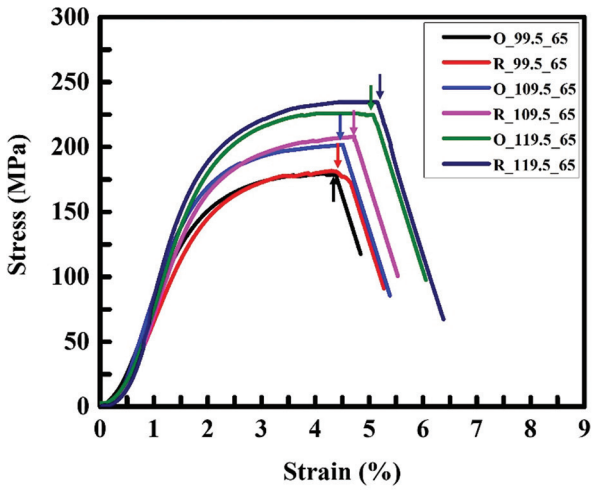

Figure 6. Compressive stress–strain curves of uniform porosity materials with different angles between the struts and with the rounded corner or not

corners, with values exceedingly twice as much. Moreover, as the stress concentration factor (k) increases, the strength has to stand for more strength by the notch. Therefore, it can be inferred that structures without rounded corners experience higher strength at the notch, leading to an earlier occurrence of the first load drop and premature crack initiation from the notch. Consequently, the crack propagation path became shorter, resulting in early fracture and a decrease in both ductility and strength.

Table 4. Mechanical properties of uniform-porosity structure fabricated by selective laser melting in this study

Specimen	Yield strength (MPa)	Compressive strength (MPa)	Strain at first load drop (%)	Strain at failure (%)	SEA (J/g)
Ti64_solid*	1213±102	1419±90	20.5	20.5	62.50
Ti64_solid	1309.67±28.11	1658.38±6.23	20.10±2.25	20.10±2.25	66.16±0.59
O_99.5_65	143.32±0.98	177.88±2.25	4.40±0.14	4.86±0.45	5.01±0.22
O_109.5_65	163.07±1.52	196.01±1.20	4.52±0.08	5.36±0.13	5.45±0.36
O_119.5_65	172.10±0.46	224.67±0.68	5.05±0.21	5.91±0.28	6.10±0.29
R_99.5_65	147.07±1.20	183.56±2.15	4.58±0.04	5.32±0.32	5.49±0.32
R_109.5_65	170.80±0.63	206.71±1.16	4.65±0.13	5.54±0.31	6.04±0.15
R_119.5_65	185.10±2.03	237.30±0.21	5.15±0.19	6.35±0.21	6.61±0.26

Note: *Mechanical properties of Ti64_solid are derived from another study,[39] for the purpose compared with the Ti64_solid printed in our laboratory.
Abbreviation: SEA: Specific energy absorption.

Table 5. Maximum strength on the node in single-porosity material

Specimen	d (mm)	ρ (mm)	k	σ (MPa)	σ_{max} (MPa)
O_99.5_65	0.71±0.01	0.16±0.01	5.21	F	5.21F
O_109.5_65	0.70±0.04	0.17±0.01	5.06	F	5.06F
O_119.5_65	0.68±0.06	0.16±0.03	5.12	F	5.12F
R_99.5_65	0.65±0.03	1.21±0.08	2.47	F	2.47F
R_109.5_65	0.66±0.05	1.25±0.04	2.45	F	2.45F
R_119.5_65	0.62±0.06	1.24±00.09	2.41	F	2.41F

However, through the compression test, we can observe the value of the difference between strain at failure and strain at first load drop, which in the rounded corner group is larger than the original group, as shown in Figure 8. This means that the structure with rounded corners could reduce the stress concentration at the node and enhance the ductility of the structure. Consequently, this causes the cracks in the rounded corner group to take longer deformation to lead the entire structure to fracture.

Besides, in reality, the specimen is a porous material, and cross-sectionally, it is not a complete circle. Upon observing the fracture of the specimen from Figure 9, it is found that the fracture surface runs along the top strut of the tetrahedral structure. Therefore, the cross-sectional area of the force applied to the specimen is corrected to 0.18 times the initial cross-sectional area, as demonstrated in Figure 10. Hence, the following analysis is based on the original force F, divided by 0.18A to obtain the corrected yield stress σ^*, representing the yield strength of a specific solid strut in the specimen. Equation IV is used to represent the maximum strength borne by a single solid structure:

$$\sigma_{max} = \sigma^* \times (1 + 2\sqrt{\frac{d}{\rho}}) \quad \text{(IV)}$$

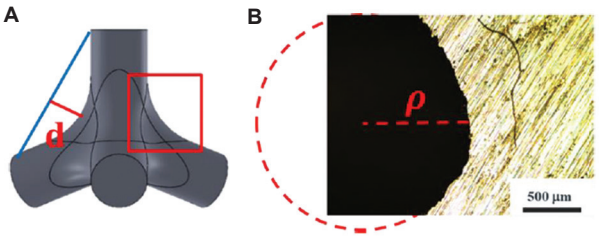

Figure 7. Demonstration of rounded corners notch depth d and curvature radius ρ in (A) CAD model and (B) magnified view of 3D printed sample of the marked area in (A). Curvature can be measured using ImageJ.

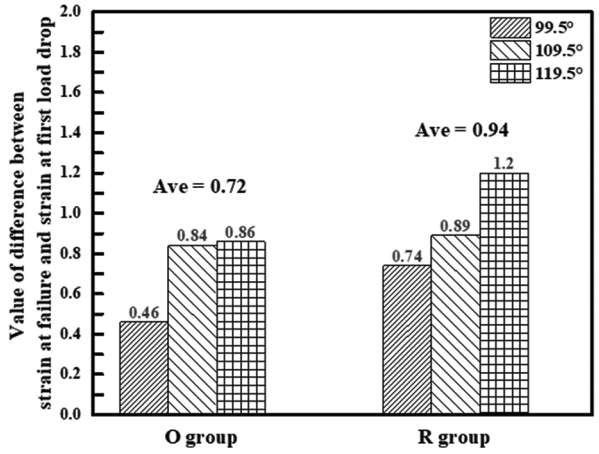

Figure 8. Value of difference between strain at failure and strain at first load drop in O group (without rounded corner) and R group (with rounded corner)

Therefore, according to the calculation results in Table 6, it can be observed that the corrected yield strength σ^* does not exceed the theoretical strength of solid Ti-6Al-4V printed by the same SLM machine, which is about 1310 MPa. However, the maximum strength σ_{max} on the notch exceeds the theoretical yield strength of 1310 MPa. This indicates that the material has reached yield at the notch, initiating plastic deformation and crack propagation,

leading to fracture at that point, resulting in a lower yield strength of the overall structure than expected.

3.3. Impact of angle between the struts on mechanical properties

Figure 6 illustrates the stress–strain curves for structures with different angles between the struts, whereas Table 4 compares the mechanical properties of structures with different support angles. According to the experimental results, structures with larger angles between the struts exhibit superior mechanical properties. Specifically, the yield strength can reach up to a maximum of 26%, and the compressive strength can reach up to 29%. In addition, they also demonstrate better energy absorption performance. Compared to the previous manipulation factor of rounded corners, structures with larger angles between the struts show greater improvements in strength.

Figure 9. Side view of specimen fracture shows the fracture on the strut node with 45°

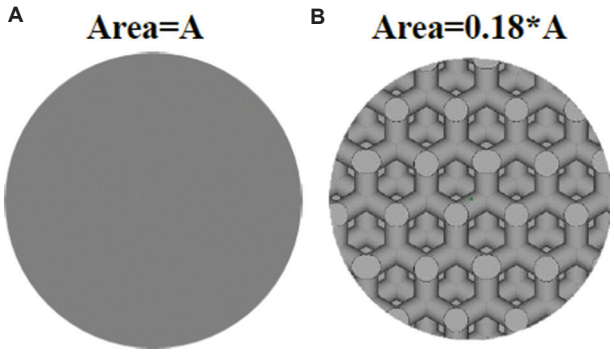

Figure 10. Test specimen cross-sectional area under compression test. (A) The area calculated by Equation II for the maximum strength of the notch; (B) the area calculated by Equation IV for the maximum strength of the notch.

When a tetrahedron is subjected to vertical compression, the strength along the strut can be divided into a buckling vector B and a bending vector D (Figure 11). Their relationship with the strut angle θ can be expressed by Equations V and VI. Furthermore, the buckling vector can be further divided into normal force N and lateral force L (Figure 12). Their relationship with the strut angle θ can be expressed by Equations VII and VIII. Combining Equations V and VI, they can be rearranged into Equations IX and X.

$$B=F \cdot \sin\theta \quad (V)$$

$$D=F \cdot \cos\theta \quad (VI)$$

$$N=B \cdot \sin\theta \quad (VII)$$

$$L=B \cdot \cos\theta \quad (VIII)$$

$$N=B \cdot \sin 2 \quad (IX)$$

$$L=B \cdot \cos\theta \cdot \sin\theta \quad (X)$$

Through the mathematical calculations presented in Table 7, it is evident that as the strut angle θ increases, lateral force L and buckling vector B increase. The increase in both the buckling vector and lateral force vectors contributes to the requirement of greater force and longer compression deformation. During compression, the material is subjected to positive compression and squeezed laterally by the structure, and the structure with a larger angle needs more deformation to achieve the angle of fracture. Consequently, when the angle between the struts becomes larger, the change in angle to achieve fracture during deformation of the tetrahedral structure also increases. This indicates that structures with larger angles require more deformation to be compressed and fracture, which also leads to the larger value of the difference between strain at failure and stain

Table 6. Maximum strength on the node of a solid strut in single porosity material

Specimen	d (mm)	ρ (mm)	k	σ (MPa)	σ^* (MPa)	σ_{max} (MPa)
O_99.5_65	0.71±0.01	0.16±0.01	5.21	143.32	796.22	4148.31
O_109.5_65	0.70±0.04	0.17±0.01	5.06	163.07	905.94	4584.06
O_119.5_65	0.68±0.06	0.16±0.03	5.12	172.10	956.11	4895.28
R_99.5_65	0.65±0.03	1.21±0.08	2.47	147.07	817.06	2018.14
R_109.5_65	0.66±0.05	1.25±0.04	2.45	170.80	948.89	2324.78
R_119.5_65	0.62±0.06	1.24±00.09	2.41	185.10	1028.33	2478.28

Table 7. Buckling vectors calculation of different angles between the struts buckling

Angle (°)	θ (°)	sinθ	cosθ	Buckling vector	Normal vector	Lateral vector
99.5	9.5	0.165	0.986	0.165F	0.027F	0.163F
109.5	19.5	0.334	0.943	0.334F	0.112F	0.315F
119.5	29.5	0.492	0.870	0.492F	0.242F	0.428F

Note: Vector can be separated by normal vector and lateral vector.

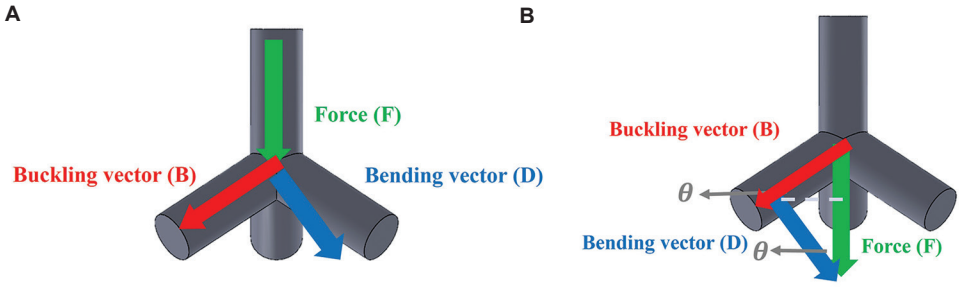

Figure 11. Demonstration of force components and angles of the tetrahedral structure. (A) The force components separated by buckling vector and bending vector; (B) the relationship between the angle between the struts and buckling vector.

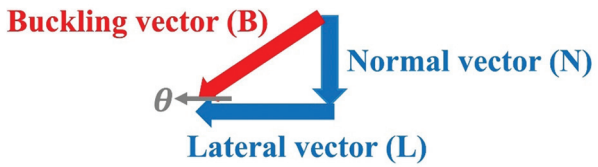

Figure 12. Buckling vector force component, which can be separated by normal vector and lateral vector

at first load drop (Figure 8). With a larger angle between the struts, the buckling vector increases, and the first load drop is delayed, resulting in a higher strain when the first strut of the entire structure fractures, accompanied by a higher strength.

3.4. Comparison between gradient material and single porosity structure

In Table 4, solid Ti-6Al-4V, without any porosity, exhibits high yield strength and ductility. However, when considering lightweight applications, gradient porous structures require less material, leading to higher SEA, as shown in Table 8. Gradient porous structures show larger strains than solid structures due to their unique collapse mechanism. The compression behavior of porous structures with uniform porosity and gradient porosity is discussed in detail below in this study.

Figure 6 and Table 8 show the stress–strain curve diagram and energy absorption of the single porosity structure, while Figure 13 and Table 8 show the stress–strain curve diagram and energy absorption of the gradient structure. Through the stress–strain curve diagram obtained from the material compression test, the area underneath can be calculated to determine the material's energy absorption. According to the experimental results, the energy absorption of the gradient material is significantly higher than that of the single porosity material. The main reason for this is that during compression, the gradient material collapses from high porosity to low porosity. As the high porosity collapses downward, it densifies the lower layers, thereby increasing strength again. This process repeats several times, leading to a layered collapse of the material, unlike the single porosity material, which fractures directly in random directions. As presented in Figure 14, two ways of different fractures between uniform porosity and gradient porosity in this experiment are shown.

Figure 15 demonstrates that as the relative density increases, the volume fraction also increases, leading to an enhancement in SEA. When compared to other studies,[40,41] the gradient structure examined in this research shows a higher energy absorption capacity at the average relative density. This indicates that optimizing the gradient structure significantly improves its energy absorption capabilities, outperforming other structural designs analyzed in previous studies.

3.5. Comparison of mechanical properties in this study

In the initial comparison between the diamond structure (O_109.5_65) and the control group (gyroid), the diamond structure showed better yield strength, whereas the gyroid exhibited superior strain and SEA (Table 9). However,

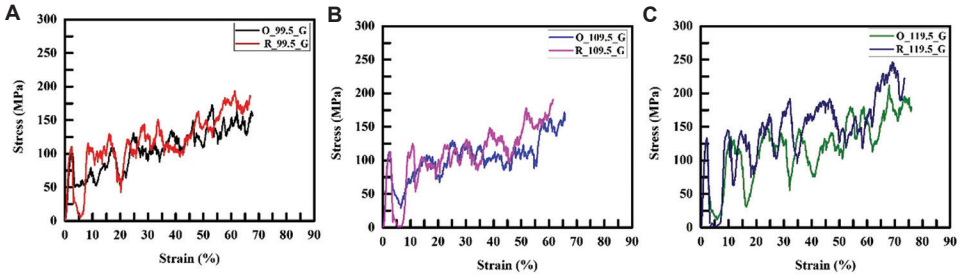

Figure 13. Compressive stress–strain curves of gradient porosity materials with angles between struts of (A) 99.5°, (B) 109.5°, and (C) 119.5°

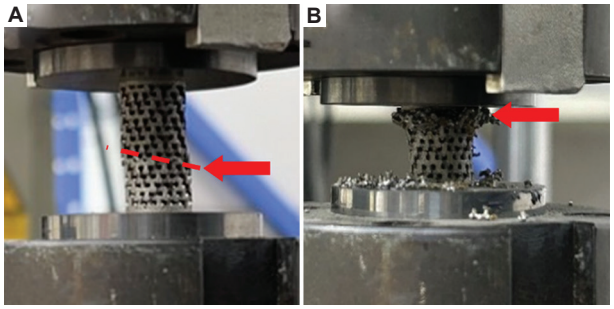

Figure 14. Compression fracture of (A) single-porosity and (B) gradient material. The deformation of the Ti-6Al-4V porous structure with single porosity occurred randomly. The gradient-porosity structure deformed from the top to the bottom layer by layer.

Table 8. Energy absorption under compression test between uniform porosity (65%) and gradient porosity (55% – 60% – 65% – 70% – 75%)

Uniform porosity	SEA (J/g)	Gradient porosity	SEA (J/g)
O_99.5_65	5.01±0.22	O_99.5_G	42.78±0.72
O_109.5_65	5.45±0.36	O_109.5_G	48.89±1.13
O_119.5_65	6.10±0.29	O_119.5_G	54.46±1.66
R_99.5_65	5.49±0.32	R_99.5_G	50.97±1.33
R_109.5_65	6.04±0.15	R_109.5_G	64.93±2.17
R_119.5_65	6.61±0.26	R_119.5_G	71.56±1.22

Abbreviation: SEA: Specific energy absorption.

after enhancing the diamond structure by adding rounded corners and increasing the angle between the struts to L_119.5_65, the yield strength increased significantly compared to the original design. When compared to the gyroid control group under gradient porosity, L_119.5_G demonstrated better energy absorption than the gyroid.

This study manipulates two main variables: The presence of rounded corners and changes in strut angles. As the radius of the rounded corners increases, the concentration of strength decreases, leading to an increase in yield strength and compressive strength. Therefore, yield strength is positively correlated with the radius of curvature of the rounded corners. As the strut angle increases, the buckling vector increases, contributing to the improvement of mechanical properties. Hence, yield strength is positively correlated with the strut angle.

The appearance of yield strength can be regarded as the starting point of plastic deformation, where the struts start to exhibit permanent deformation. The appearance of compressive strength reveals the beginning of strut fracture. In this experiment, the sizes of the strut angles were compared for both yield strength and compressive strength. As the strut angle increases, both yield strength and compressive strength increase accordingly. As the y-axis shown in Figure 16, the enhancement of yield strength and compressive strength with different angles between the struts up to 26% and 29%, respectively. The increase in strut angle contributes significantly to the improvement of mechanical properties.

However, despite the increase in stress concentration factor, the strength standing by the notch increases accordingly. Conversely, both yield strength and compressive strength decrease, but the magnitude of the difference on the y-axis is not significant, with only a 6% and 8% difference, respectively. From Figure 17, it can be observed that the majority of the differences in mechanical properties still stem from changes in the angle. Hence, the strut angle with the maximum value of 119.5° is consistently depicted at the top of the graph.

Furthermore, by multiplying the reciprocal of the two manipulated variables in this experiment, namely the strut angle and the stress concentration factor, as the x-axis and setting the y-axis as the yield strength, Figure 18 was obtained. It can be observed that they exhibit a positive correlation, with correlation coefficients (R^2) all >0.95. This indicates a minimal error, affirming the reliability of the data.

Figures 19 and 20 show that, through different scales of photography, both camera and optical microscope reveal clear differences in image results between specimens with and without rounded corners. However, specimens with rounded corners do not exhibit significant improvements in yield strength and compressive strength compared to

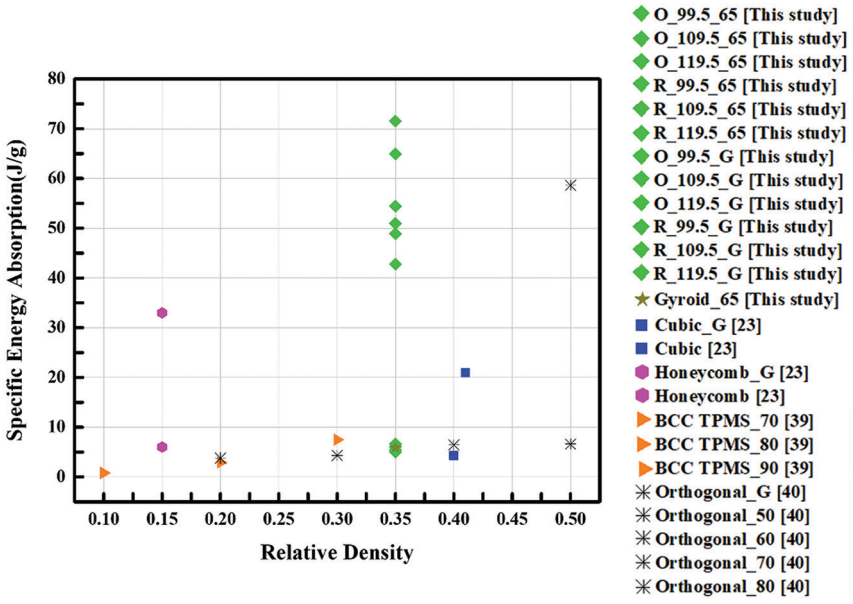

Figure 15. Comparison of the specific energy absorption with other porous structures built by selective laser melting. The black one indicates the gradient porosity; the gray one indicates the uniform porosity.

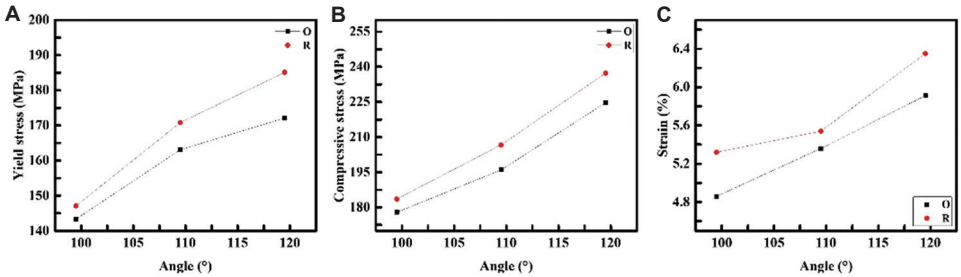

Figure 16. Compression test of (A) Yield strength, (B) Compressive strength, and (C) strain versus angle between the struts. O=the original sample, without rounded corners; R=the same with rounded corners.

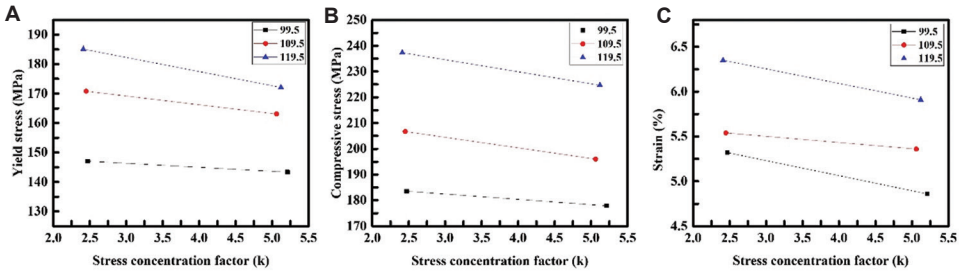

Figure 17. Compression test of (A) yield strength, (B) compressive strength, and (C) strain versus stress concentration factor

Table 9. Summary comparison under compression test in this study

Specimen	Yield strength (MPa)	Compressive strength (MPa)	Strain (%)	SEA (J/g)
Gyroid_65	155.9±3.5	210.8±0.2	6.3±0.5	5.9±0.2
O_109.5_65	163.1±1.5	196.0±1.2	5.5±0.1	5.5±0.4
R_119.5_65	185.1±2.0	237.3±0.2	6.4±0.2	6.6±0.3
R_119.5_G	135.4±3.3	249.3±3.1	74.7±1.8	71.6±1.2

Abbreviation: SEA: Specific energy absorption.

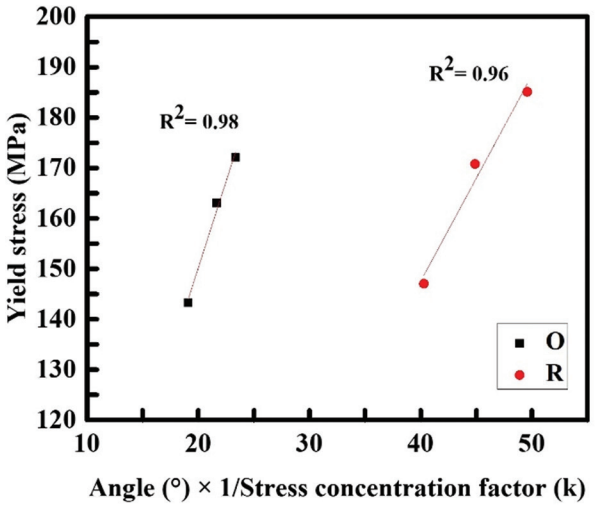

Figure 18. Yield strength versus different angles between the struts and stress concentration factor (k). The correlation coefficients (R^2) all >0.95 show the reliability of the data in this experiment. O=the original sample, without rounded corners; R=the sample with rounded corners.

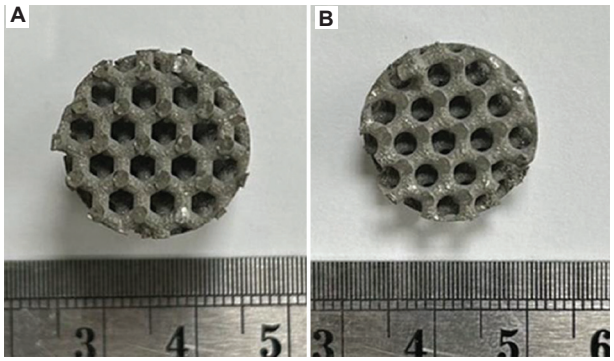

Figure 19. Top view of the specimen taken with the camera (A) without rounded corners and (B) with rounded corners

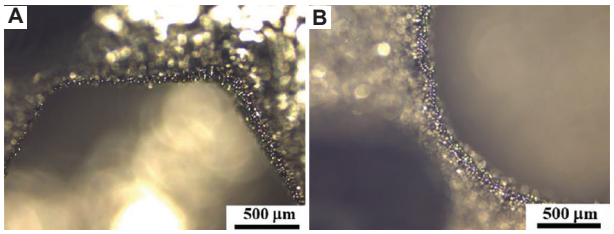

Figure 20. Optical microscope images for the top view of the specimen (A) without rounded corners and (B) with rounded corners

those without rounded corners. This is speculated to be due to the lack of post-processing of the specimens, as evidenced by the unmelted powder adhering to the struts (Figure 21). Despite the structure with rounded corners, this adherence results in substantial surface roughness, leading to stress concentration effects and eventual material failure. If the surface roughness can be reduced in the future, thereby reducing strength concentration issues, the mechanical properties of the structure are expected to improve once again.[42]

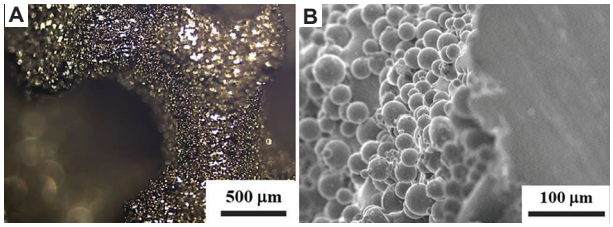

Figure 21. Unmelted powder attached on strut under (A) optical microscope and (B) scanning electron microscope

4. Conclusion

In this study, gradient porous structures and geometric optimization strategies were employed to enhance mechanical performance. Gradient porosity not only reduced sample weight but also significantly increased SEA due to layer-by-layer collapse behavior. In addition, increasing the angle between struts improved ductility and delayed structural failure, leading to enhancements in yield strength and compressive strength by approximately 26% and 29%, respectively. Node chamfering helped to reduce stress concentration and resulted in yield and compressive strength improvements of about 6 – 8%; however, its effect was limited, likely due to surface roughness caused by unmelted powder.

Furthermore, compared to the previously validated gyroid_65% structure, the optimized diamond-based design (L_119.5_65%) exhibited a 19% increase in strength, as shown in Table 9. These findings indicate that the combined implementation of gradient porosity and geometric optimization is an effective strategy for designing high-performance porous metallic structures for energy absorption applications.

Acknowledgments

The authors are grateful for the support of the Taiwan Space Agency and China Steel Corporation.

Funding

The authors gratefully acknowledge the sponsorship support from the National Science and Technology Council of Taiwan, ROC, under project no. NSTC 112-2221-E-110-019.

Conflict of interest

Che-Nan Kuo is an Editorial Board Member of this journal but was not in any way involved in the editorial and peer-review process conducted for this paper, directly

or indirectly. Separately, other authors declared that they have no known competing financial interests or personal relationships that could have influenced the work reported in this paper.

Author contributions

Conceptualization: Yu-Yao Chan, Che-Nan Kuo
Formal analysis: Yu-Yao Chan, Yi Chao
Investigation: Yu-Yao Chan, Yi Chao
Methodology: Yu-Yao Chan, Che-Nan Kuo
Writing – original draft: Yu-Yao Chan
Writing – review & editing: Che-Nan Kuo

Ethics approval and consent to participate

Not applicable.

Consent for publication

Not applicable.

Availability of data

The authors confirm that the data supporting the findings of this study are available within the article.

References

1. Simonelli M, Tse YY, Tuck C. The formation of α+ β microstructure in as-fabricated selective laser melting of Ti-6Al-4V. *J Mater Res*. 2014;29(17):2028-2035.

   doi: 10.1557/jmr.2014.166

2. Cui C, Hu B, Zhao L, Liu S. Titanium alloy production technology, market prospects and industry development. *Mater Design*. 2011;32(3):1684-1691.

   doi: 10.1016/j.matdes.2010.09.011

3. Liu S, Shin YC. Additive manufacturing of Ti6Al4V alloy: A review. *Mater Design*. 2018;164:107552.

   doi: 10.1016/j.matdes.2018.107552

4. Donachie MJ. *Titanium: A Technical Guide*. 2nd ed. Netherlands: ASM International; 2000.

   doi: 10.31399/asm.tb.ttg2.9781627082693

5. Li Y, Feng Z, Hao L, *et al*. A review on functionally graded materials and structures via additive manufacturing: From multi-scale design to versatile functional properties. *Adv Mater Technol*. 2020;5(6):1900981.

   doi: 10.1002/admt.201900981

6. Allen J. An investigation into the comparative costs of additive manufacture vs. Machine from solid for aero engine parts. *Cost Eff Manuf via Net-Shape Process*. 2006;17:1-17.

7. O'Leary R, Setchi R, Prickett P, Hankins G, Jones N. An investigation into the recycling of Ti-6Al-4V powder used within SLM to improve sustainability. *Impact J Innov Impact*. 2016;8(2):377.

8. Kas M, Yilmaz O. Radially graded porous structure design for laser powder bed fusion additive manufacturing of Ti-6Al-4V alloy. *J Mater Process Technol*. 2021;296:117186.

   doi: 10.1016/j.jmatprotec.2021.117186

9. Zhang W, Xu J. Advanced lightweight materials for automobiles: A review. *Mater Design*. 2022;221:110994.

   doi: 10.1016/j.matdes.2022.110994

10. Lv X, Xiao Z, Fang J, Li Q, Lei F, Sun G. On safety design of vehicle for protection of vulnerable road users: A review. *Thin-Walled Struct*. 2023;182:109990.

    doi: 10.1016/j.tws.2022.109990

11. Huang R, Riddle M, Graziano D, *et al*. Energy and emissions saving potential of additive manufacturing: The case of lightweight aircraft components. *J Clean Prod*. 2016;135:1559-1570.

    doi: 10.1016/j.jclepro.2015.04.109

12. Uhlmann E, Kersting R, Klein TB, Cruz MF, Borille AV. Additive manufacturing of titanium alloy for aircraft components. *Procedia Cirp*. 2015;35:55-60.

    doi: 10.1016/j.procir.2015.08.061

13. Zochowski P, Bajkowski M, Grygoruk R, *et al*. Ballistic impact resistance of bulletproof vest inserts containing printed titanium structures. *Metals*. 2021;11(2):225.

    doi: 10.3390/met11020225

14. Brennan-Craddock J, Brackett D, Wildman R, Hague R. The design of impact absorbing structures for additive manufacture. *J Phys Conf Ser*. 2012;382:012042.

    doi: 10.1088/1742-6596/382/1/012042

15. Pan C, Han Y, Lu J. Design and optimization of lattice structures: *A review. Appl Sci*. 2020;10(18):63-74.

    doi: 10.3390/app10186374

16. Park KM, Min KS, Roh YS. Design optimization of lattice structures under compression: Study of unit cell types and Cell arrangements. *Materials*. 2022;15:97.

    doi: 10.3390/ma15010097

17. Thompson SM, Bian L, Shamsaei N, Yadollahi A. An overview of direct laser deposition for additive manufacturing; part I: Transport phenomena, modeling and diagnostics. *Addit Manuf*. 2015;8:36-62.

    doi: 10.1016/j.addma.2015.07.001

18. Yap CY, Chua CK, Dong ZL, *et al*. Review of selective laser melting: Materials and applications. *Appl Phys Rev*. 2015;2(4):041101.

    doi: 10.1063/1.4935926

19. Khorasani A, Gibson I, Awan US, Ghaderi A. The effect

of SLM process parameters on density, hardness, tensile strength and surface quality of Ti-6Al-4V. *Addit Manuf*. 2019;25:176-186.

doi: 10.1016/j.addma.2018.09.002

20. Shifeng W, Shuai L, Qingsong W, Yan C, Sheng Z, Yusheng S. Effect of molten pool boundaries on the mechanical properties of selective laser melting parts. *J Mater Process Technol*. 2014;214(11):2660-2667.

doi: 10.1016/j.jmatprotec.2014.06.002

21. Ansari MJ, Nguyen DS, Park HS. Investigation of SLM process in terms of temperature distribution and melting pool size: Modeling and experimental approaches. *Materials*. 2019;12(8):1272.

doi: 10.3390/ma12081272

22. Seetoh IP, Liu X, Markandan K, Zhen L, Lai CQ. Strength and energy absorption characteristics of Ti6Al4V auxetic 3D anti-tetrachiral metamaterials. *Mech Mater*. 2021;156:103811.

doi: 10.1016/j.mechmat.2021.103811

23. Choy SY, Sun CN, Sin WJ, *et al*. Superior energy absorption of continuously graded microlattices by electron beam additive manufacturing. *Virtual Phys Prototyp*. 2021;16(1):1-15.

doi: 10.1080/17452759.2020.1868656

24. Mahamood RM, Akinlabi ET, Owolabi MG, Abdulrahman KO. Advanced manufacture of compositionally graded composite materials: An overview. In: *Hierarchical Composite Materials: Materials, Manufacturing, Engineering*. Berlin, Boston: De Gruyter; 2019. p. 41-54.

doi: 10.1515/9783110545104-003

25. Evans AG, He MY, Deshpande VS, Hutchinson JW, Jacobsen AJ, Carter WB. Concepts for enhanced energy absorption using hollow micro-lattices. *Int J Impact Eng*. 2010;37:947-959.

doi: 10.1016/j.ijimpeng.2010.03.007

26. Liu F, Zhang DZ, Zhang P, Zhao M, Jafar S. Mechanical properties of optimized diamond lattice structure for bone scaffolds fabricated via selective laser melting. *Materials*. 2018;11:374.

doi: 10.3390/ma11030374

27. Zhao M, Zhang DZ, Liu F, Li Z, Ma Z, Ren Z. Mechanical and energy absorption characteristics of additively manufactured functionally graded sheet lattice structures with minimal surfaces. *Int J Mech Sci*. 2020;167:105262.

doi: 10.1016/j.ijmecsci.2019.105262

28. Sun Q, Sun J, Guo K, Wang L. Compressive mechanical properties and energy absorption characteristics of SLM fabricated Ti6Al4V triply periodic minimal surface cellular structures. *Mech Mater*. 2022;166:104241.

doi: 10.1016/j.mechmat.2022.104241

29. Zhao X, Li Z, Zou Y, Zhao X. Compressive characteristics and energy absorption capacity of automobile energy-absorbing box with filled porous TPMS structures. *Appl Sci*. 2024;14(9):3790.

doi: 10.3390/app14093790

30. Li Z, Zhao R, Chen X, Jiao Y, Chen Z. Design approach for tuning the hybrid region of 3D-printed heterogeneous structures: Modulating mechanics and energy absorption capacity. *ACS Appl Mater Interfaces*. 2023;15(6):7686-7699.

doi: 10.1021/acsami.2c17753

31. Dong JH, Wang YJ, Jin FN, Fan HL. Crushing behaviors of buckling-induced metallic meta-lattice structures. *Def Technol*. 2022;18(8):1301-1310.

doi: 10.1016/j.dt.2021.07.014

32. Obadimu SO, Kourousis KI. Compressive behaviour of additively manufactured lattice structures: *A review. Aerospace*. 2021;8(8):207.

doi: 10.3390/aerospace8080207

33. Li Y, Wang XS, Meng XK. Buckling behavior of metal film/substrate structure under pure bending. *Appl Phys Lett*. 2008;92(13):131902.

doi: 10.1063/1.2897035

34. Zhao S, Li SJ, Hou WT, Hao YL, Yang R, Misr RDK. The influence of cell morphology on the compressive fatigue behavior of Ti-6Al-4V meshes fabricated by electron beam melting. *J Mech Behav Biomed Mater*. 2016;59:251-264.

doi: 10.1016/j.jmbbm.2016.01.034

35. Li D, Liao W, Dai N, Xie YM. Comparison of mechanical properties and energy absorption of sheet-based and strut-based gyroid cellular structures with graded densities. *Materials*. 2019;12(13):2183.

doi: 10.3390/ma12132183

36. Yang E, Leary M, Lozanovski B, *et al*. Effect of geometry on the mechanical properties of Ti-6Al-4V Gyroid structures fabricated via SLM: A numerical study. *Mater Design*. 2019;184:108165.

doi: 10.1016/j.matdes.2019.108165

37. Choy SY, Sun CN, Leong KF, Wei J. Compressive properties of Ti-6Al-4V lattice structures fabricated by selective laser melting: Design, orientation and density. *Addit Manuf*. 2017;16:213-224.

doi: 10.1016/j.addma.2017.06.012

38. Jenkins SNM. *Mechanical Properties and Structural Evaluation of Diamond Structure Ti6Al4V Lattices Made by Electron Beam Melting*. England: University of Sheffield; 2017.

39. Kurdi A, Basak AK. Micro-mechanical behaviour of selective laser melted Ti6Al4V under compression. *Mater Sci Eng A*. 2021;826:141975.

doi: 10.1016/j.msea.2021.141975

40. Zhao M, Liu F, Fu G, Zhang DZ, Zhang T, Zhou H. Improved mechanical properties and energy absorption of BCC lattice structures with triply periodic minimal surfaces fabricated by SLM. *Materials*. 2018;11(12):2411.

doi: 10.3390/ma11122411

41. Wang YP, Kuo CN. Research on energy absorption of gradient porosity structural materials. *Mater Today Proc*. 2022;70:578-582.

doi: 10.1016/j.matpr.2022.09.594

42. Kuo CN, Wang YP, Chua CK. Effect of electropolishing on mechanical property enhancement of Ti6Al4V porous materials fabricated by selective laser melting. *Virtual Phys Prototyp*. 2022;17(4):919-931.

doi: 10.1080/17452759.2022.2090383